Relativistic Model of D-^{3}He Fuel in ICF using KrF Laser Pulses with Circular Polarization

M G Shabankareh[1], S N Hosseinimotlagh[2]* and N Farhangkhah[3]

[1,2,3]Department of Physics, Shiraz Branch, Islamic Azad University, Shiraz, Iran

Abstract

Laser ponderomotive force at ultra-high intensities provides an efficient ion acceleration in bulk dense targets and evacuates a channel enabling further laser beam propagation. The developed quasi-stationary model of a laser piston—a double layer structure supported by the radiation pressure—predicts the general parameters of the acceleration process in homogeneous and inhomogeneous over-dense plasmas. In the first step of this work we solve the dynamics equations of Krypton-Fluoride (KrF) laser with an operating wavelength of 248 nm has the deepest ultraviolet (UV) wavelength of all current candidates for laser drivers. These qualities provide fundamental advantages to obtaining robust high gain implosions by means of direct drive. Then in the second step, using the obtained expression for the piston velocity, we determine the energy of the accelerated ions, their energy distribution, and the laser penetration depth in case of an inhomogeneous plasma slab. This way we can estimate the laser parameters necessary for propagating the light wave up to a certain density. Moreover, we present solutions for the governing equations describing the detailed structures of the ion charge separation layer and the electron sheath of the piston. Results of our work are presented for circular polarization and various intensities of the incident laser light, which exposes homogeneous plasma slabs of different densities. Although the calculations confirm the basic features of the analytical model, they show two overlaying nonstationary effects: nonlinear oscillations of the piston parameters around the stationary values and strong radiative energy losses of accelerated electrons in ultra-intense laser fields at low plasma density. These nonstationary features modify the stationary piston regime and set the limits on its validity.

Keywords: KrF Laser, ponderomotive force, Relativistic, Polarization, fusion

1-Introduction

Inertial confinement fusion (ICF) is a type of fusion energy research that attempts to initiate nuclear fusion reactions by heating and compressing a fuel target, typically in the form of a pellet that most often contains a mixture of deuterium and tritium. To compress and heat the fuel, energy is delivered to the outer layer of the target using high-energy beams of laser light, electrons or ions, although for a variety of reasons, almost all ICF devices as of 2015 have used lasers. The heated outer layer explodes outward, producing a reaction force against the remainder of the target, accelerating it inwards, compressing the target. This process is designed to create shock waves that travel inward through the target. A sufficiently powerful set of shock waves can compress and heat the fuel at the center so much that fusion reactions occur. The energy released by these reactions will then heat the surrounding fuel, and if the heating is strong enough this could also begin to undergo fusion. The aim of ICF is to produce a condition known as "ignition", where this heating process causes a chain reaction that burns a significant portion of the fuel. Typical fuel pellets are about the size of a pinhead and contain around 10 milligrams of fuel: in practice, only a small proportion of this fuel will undergo fusion, but if all this fuel were consumed it would release the energy equivalent to burning a barrel of oil. We believe that direct drive with a Krypton-Fluoride (KrF) laser is an attractive candidate for inertial fusion energy (IFE) because KrF laser beams are very uniform. KrF lasers

have outstanding beam spatial uniformity, which reduces the seed for hydrodynamic instabilities; they have an inherent short wavelength (248 nm) that increases the rocket efficiency and raises the threshold for deleterious laser-plasma instabilities; and they have the capability for "zooming" the spot size to follow an imploding pellet and thereby increase efficiency. The cost to develop a KrF laser for inertial fusion energy would be relatively modest because of the modularity of the system. We have a conceptual design for a 5000 J Rep-rate KrF facility that would enable us to address some of the key engineering issues for inertial fusion energy.

Also in this paper we present a more detailed analysis of the quasi-stationary regime of ion acceleration in the laser piston, applying analytical methods. In the analytical model we describe the internal structure of the laser piston assuming complete plasma evacuation in the vicinity of the traveling laser wave. This paper is organized in the following way. After a short introduction, we give an aneutronic clean D-^{3}He fusion reaction in section 2. In section 3, dynamics behavior of KrF lasers are presented. In section 4, an analytical description of the relativistic piston motion driven by the ponderomotive pressure of a circularly polarized laser wave are presented. Finally, we summarize our main results and suggest directions of further investigations.

2. Aneutronic clean D-^{3}He Fusion Reaction

To achieve an absolutely "clean" reactor, one would have to use one of the other possible fusion reactions listed in Table 1.

Table 1. List of possible fusion reactions

Reaction
$D + T \rightarrow He^4(3.52MeV) + n(14.06MeV)$
$D + D \rightarrow T^3(1.01MeV) + p(3.03MeV)$
$D + D \rightarrow He^3(0.82MeV) + n(2.45MeV)$
$D + He^3 \rightarrow He^4(3.67MeV) + p(14.67MeV)$
$T + T \rightarrow He^4 + n + n(11.32MeV)$
$He^3 + T \rightarrow He^4 + p + n(12.1MeV)$
$He^3 + T \rightarrow He^4(4.8MeV) + D(9.5MeV)$
$He^3 + T \rightarrow He^5(2.4MeV) + p(11.9MeV)$
$p + Li^6 \rightarrow He^4(1.7MeV) + He^3(2.3MeV)$
$p + Li^7 \rightarrow 2He^4(22.4MeV)$
$D + Li^6 \rightarrow 2He^4(22.4MeV)$
$p + B^{11} \rightarrow 3He^4(8.082MeV)$
$n + Li^6 \rightarrow He^4(2.1MeV) + T(2.7MeV)$

The D-D fusion reaction is one of the side reactions of D-^{3}He, which is carried out through two channels b and c with almost the same probability, but since the reactivity of these two channels is much lower than D-^{3}He, the amount of neutron production and tritium is not significant from these channels. It is also necessary to mention that because the D-T fusion reaction is one of the side reactions, it produces neutrons with low rate. Another aneutronic fusion reaction is P-^{11}B. The side effects of tritium generation and the production of high-energy neutrons have aroused interest in using aneutronic reactions. Possible candidates for these reactions are D-^{3}He and p-^{11}B. But from comparing their reactivities rate, it can be seen that the D-^{3}He reaction is more attractive than the p-^{11}B because D-^{3}He requires a lower temperature than p-^{11}B reaction. Although it should be emphasized that both of them require much higher temperatures and triple product than the D-T reaction. But it should be noted that there is still disagreement about the feasibility of the p-^{11}B reaction. However, research on p-^{11}B continues in earnest. In the range of temperatures 0.5–190 keV the reactivity of D^{3}He reaction is accurately fitted by

the functional form (Bosch and Hale 1992): $\langle \sigma v \rangle = C_1 \zeta^{-5/6} \xi^2 \exp\left(-3\zeta^{1/3}\xi\right)$ Where: $\zeta = 1 - \frac{C_2 T + C_4 T^2 + C_6 T^3}{1 + C_3 T + C_5 T^2 + C_7 T^3}$ and ξ can be written as : $\xi = C_0/T^{1/3}$. The values of the constant C_0 and of the fit coefficients C_1–C_7 appearing in above equations are: $C_0 \left(keV^{1/3}\right) = 10.572, C_1 \times 10^{16} \left(cm^3/s\right) = 151.16, C_2 \times 10^3 (keV^{-1}) = 6.4192, C_3 \times 10^3 (keV^{-1}) = -2.0290, C_4 \times 10^3 (keV^{-2}) = -0.019108$, $C_5 \times 10^3 (keV^{-2}) = 0.13578$, $C_6 \times 10^3 (keV^{-3}) = 0$, $C_7 \times 10^3 (keV^{-3}) = 0$, in the temperature range 0.5-190keV .

But due to the higher reactivity of the aneutronic fusion reaction of D-^{3}He compared to p-^{11}B, this reaction has been investigated in this article. It is necessary to mention that the amount of ^{3}He on the surface of the earth is not very high so it cannot produce enough fusion energy. While on the surface of the moon, the amount of ^{3}He is so much that it can provide the energy needed by humans for many years, and the origin of the presence of ^{3}He on the surface of the moon is the solar wind. The abundance of ^{3}He on the lunar surface has been determined by analyzing lunar samples brought back by the Apollo and Luna missions. Also, in the atmosphere of giant gas planets, the amount of ^{3}He is so much that it can produce the energy needed by humans for about 10^{17} years. But extracting ^{3}He from these sources and transferring it to the earth will be very difficult and expensive and can only be achieved in the distant future [16].

There is also ^{3}He in natural gas wells. However, at the current rate of natural gas use, this source provides ^{3}He less than 5 kg/year. Also, ^{3}He can be produced from the radioactive decay of ^{3}H in reactors. Large amounts of ^{3}He also exist in the Earth's mantle but are inaccessible. Therefore, a combination of artificial and natural sources of ^{3}He on earth can provide sufficient ^{3}He fuel for the development of D-^{3}He fusion technology.

How can solid ^3He be produced? In response, it should be said that the world is full of solid helium in polymorphic forms. Therefore, the exploration of helium *allotropes* is vital to our understanding of nature. However, producing, observing, and using solid helium on the earth is challenging because high-pressure techniques are required to solidify helium. Of course, one of the ways to produce solid ^3He at room temperature is through the encapsulation effect of the diamond network. For more studies, refer to reference [17].

It is also characteristic of the D-^{3}He reaction that the protons released in this reaction can heat the fuel ions not only due to soft Coulomb collisions but also through elastic scattering on the nuclear optical potential, which is called the nuclear elastic scattering (NES) process. This scattering process occurs in relatively short distances and involves high momentum transfer. As a result, energetic nuclei, which are the fuel ions D and ^{3}He, appear in the plasma. This leads to average growth of the fusion reaction rate and thus contributes to the growth of the total energy release of the thermonuclear process. This is another reason that has encouraged the authors of this article to choose aneutronic D-^{3}He fuel.

### 3-Dynamics behavior of KrF lasers

An implosion directly driven by a laser was one of the earliest concepts proposed to achieve inertial confinement fusion (ICF) and remains the most straightforward. [1] The Krypton-Fluoride (KrF) laser with an operating wavelength of 248 nm has the deepest ultraviolet (UV) wavelength of all current candidates for laser drivers and it has demonstrated the most uniform illumination. These qualities provide fundamental advantages to obtaining robust high gain implosions by means of direct drive. Recent target design innovations can further mitigate the

challenge posed by hydrodynamic instability. A particularly promising new approach to direct drive is shock ignition. [2] Simulations indicate that shock ignition can obtain the very high gains projected for fast ignition but with a simpler laser and target configuration. [3-4] NRL simulations indicate gains greater than 100 are feasible with a 500 kJ laser and gains potentially above 200 are possible at energies of 1 MJ when utilizing a KrF driver. [4]

Advantages of KrF for the achievement of high gain target implosions have been recognized for many years. [1] However, it was viewed as a challenging laser technology to implement compared to the ubiquitous flash lamp-pumped Nd:glass lasers that are currently used throughout the world for ICF research. Large KrF systems use high power electron beams to excite a gaseous lasing medium. Obtaining good performance from such amplifiers poses both physics and technological challenges. Nevertheless, the laser fusion program at NRL has made significant progress in advancing the state of the art in efficiency, performance and durability of large electron beam pumped KrF lasers by the development of two large scale systems. The original system, the Nike laser, is an integrated laser-target facility and is the world"s largest KrF laser. [5] It has produced up to 5 kJ of laser light in 56 angularly multiplexed beams. The beam smoothing by induced spatial incoherence (ISI) that was implemented on Nike has also allowed an ability to zoom the focal diameter of the laser beams during a pulse. [6-7] This unique feature would be used to match the drive laser focal spot to the diameter of an imploding pellet to increase the overall laser-target coupling efficiency. The newer facility at NRL, the Electra laser, was designed to develop technologies that can meet the fusion energy requirements for rep-rate, efficiency, durability, and cost. [8] The 30 cm aperture main amplifier of Electra provides up to 700 J of laser energy and has demonstrated high transport efficiency (>70%) of the electron beam into the laser gas. The Electra laser has also demonstrated 50,000 shots continuous at 5 Hz and 90,000 shots at 2.5 Hz with technologies that are scalable to a full scale (> 16 kJ) amplifier. The overall system efficiency is predicted to be greater than 7% based on advances in the electron beam transport into the gas and the KrF kinetics. This level is adequate for inertial confinement fusion systems based on the high gains predicted for the advanced KrF driven implosion designs cited above. The combination of good target and driver performance makes direct drive with KrF lasers an attractive choice for inertial confinement fusion energy. The ongoing laser fusion program at NRL has four major objectives: (i) understanding and quantifying the benefits of KrF drivers,(ii) developing the high performance ICF target designs through theoretical analysis and computer simulations, (iii) conducting experimental studies of hydrodynamics and laser-plasma instabilities in targets driven by a KrF laser, and (iv) addressing the basic scientific and technological issues in the production and operation of advanced electron-beam pumped KrF lasers for the longer term energy application. This paper will briefly describe the first three goals related to the continued advances in target physics being made at NRL through theory and experiment. Nike is a high-energy krypton-fluoride (KrF) laser that was primarily developed to study the physics and means for control of hydrodynamic instability. The KrF laser has unique characteristics for such experiments, particularly in regard to beam smoothing technology. Nike produces the most uniform target illumination of all available high-energy UV lasers (at 1/3 or 1/4 μm). The Nike laser at the United States Naval Research Laboratory in Washington DC is a 56 beam, 4-5 kJ per pulse electron beam pumped krypton fluoride excimer laser which operates in the ultraviolet at 248 nm with pulse widths of a few nanoseconds. Nike was completed in the late 1980s and is used for investigations into inertial confinement fusion. By using a KrF laser with induced spatial incoherence (ISI) optical smoothing, the modulations in the laser focal profile (beam intensity anisotropy) are only 1% in one beam and < 0.3% with a 44-beam overlap. This feature is especially important for minimizing the seeding of Rayleigh-Taylor instabilities in the imploding fusion target capsule plasma.

We know that, KrF lasers are a particular type of excimer lasers. Excimer lasers are rare-gas halide lasers emitting in the ultraviolet, that operate via the electronic transitions of molecules. Electra uses an Ar/Kr/F2 laser gas mixture and emits at a wavelength of 248nm (Fig.2).
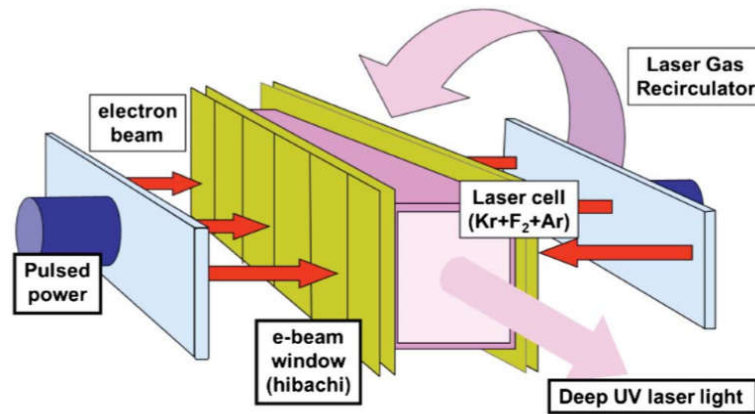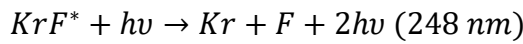
The dominant formation reactions are:

$Kr^* + F_2 \rightarrow KrF^* + F$
$ArF^* + Kr \rightarrow KrF^* + Ar$
$Kr^+ + F^- + M \rightarrow KrF^* + M$
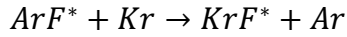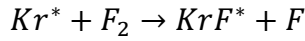
Emission occurs when:

$KrF^* + h\upsilon \rightarrow Kr + F + 2h\upsilon \ (248 \ nm)$

Figure 1: The principal components of an electron beam pumped KrF laser

The system of equations that are used to describe the incoherent amplification of laser pulses in KrF media is in the form:

$$\frac{dN_L}{dt} = -\frac{N_L - \Theta N_B}{\tau_\upsilon} - \frac{\Theta_C N_L - \Theta_B N_K}{\tau_{BC}} - \frac{N_L}{\tau_L} - \sigma N_L I \qquad (1)$$

$$\frac{dN_K}{dt} = -\frac{N_K - \Theta N_C}{\tau_\upsilon} - \frac{\Theta_B N_K - \Theta_C N_L}{\tau_{BC}} - \frac{N_K}{\tau_K} \qquad (2)$$

$$\frac{dN_B}{dt} = \alpha R - \frac{\Theta_C N_B - \Theta_B N_C}{\tau_\upsilon} - \frac{N_B}{\tau_B} - \sigma N_L I \qquad (3)$$

$$\frac{dN_C}{dt} = \beta R - \frac{\Theta_B N_C - \Theta_C N_B}{\tau_\upsilon} - \frac{N_C}{\tau_C} \qquad (4)$$

$$\frac{\partial I}{\partial x} + \frac{1}{c}\frac{\partial I}{\partial t} = (\sigma N_L - \rho)I \qquad (5)$$

Where $N_L = \sum_{\upsilon=0}^{1} N_{B\upsilon}$ and $N_K = \sum_{\upsilon=0}^{1} N_{C\upsilon}$ are the sums of population of the laser levels in the B-state and corresponding levels in the C-state (the population of the L and K state respectively); τ_υ is the vibrational relaxation time for the L and K state; $\Theta = \sum_{\upsilon=0}^{1} \Theta_\upsilon$; τ_L and τ_K are the decay time of the L and K state, respectively. An exact description of the generation process in the excimer laser requires Eqs.1-5 to be solved simultaneously with the equations describing the kinetics of formation and quenching of excimer molecules. In particular, it enables determination of the dynamics of collisional relaxation times and absorptive losses of the medium and determination of the exact form of the R(t) function. Because, in the analyzed

case of short pulse generation, the actual form of the R(t) function is of the secondary importance and the changes in relaxation times and losses can be accepted as slow, it was assumed in the model that the R(t) function is given and relaxation times and medium losses are fixed. The R(t) function was assumed in the form R = R0 exp [-(t/Tp) ^{4}] while the numeral values of the medium parameters were taken typical for KrF laser, and especially: $\tau_B = \tau_C = \tau_L = \tau_K = 1.5\ ns, \tau_L^S = 8\ ns, \tau_v = 1\ ns, \sigma = 2.4 \times 10^{-16}\ cm^2, \rho = 0.01\ cm^{-1}, \alpha = \beta = 0.5, \Theta_B = 0.72, \Theta_C = 0.28$. In our model, as the accessible vibrational levels of the *KrF*(B)* state, we took the levels $v = 0,1$. Their calculation showed that the vibrational populations in $v = 0,1$ can all be extracted efficiently. However, the vibrational quantum number dependence on its accessibility makes the model complex and also the consideration of their gain spectrum widths is necessary. Therefore, for simplicity, we ignored the contribution of higher vibrational. Because the quantity of characteristic time constant of τ_v depends on the vibrational quantum number considered, the τ_v obtained in this paper is only valid for the model with the accessible levels of $v = 0,1$. The quantities of $\Theta_B, \Theta_C, and\ \Theta$ are calculated by the energy gaps of $E_B - E_C = 80\ cm^{-1}\ and\ \Delta E_v = 327\ cm^{-1}$ and the instantaneous gas temperature. By solving Eqs.1-5 the population of the levels B and C as well as the vibration levels of them were calculated that are shown in Fig.1. As presented in Fig.2 the population inversion of levels after time 5 ns reaches saturation. The gain recovery curve $g(t) = \sigma N_l(t)$ for the KrF amplifier obtained from Eqs.1-5 at the parameters given above is presented in Fig.3.Our value for the saturation energy density equals to $E_{sat} = \frac{hc}{\lambda \sigma} = 32\ \frac{j}{m^2}$ and for I_{sat} as shown in Fig.5 with solving Eqs.1-5 is obtained $I_{sat} = 3.2 \times 10^{14}\ \frac{W}{m^2}$ and this value equals to $I_{sat} = \frac{E_{sat}}{\tau} = \frac{hc}{\lambda \sigma \tau} = 3.2 \times 10^{14}\ \frac{W}{m^2}$. A fusion driver needs much larger systems (3-5 kJ, pulses of 20–1000 ns). Here our amplifier system as presented in Fig.4 is routinely operated with maximum intensity $2.2 \times 10^{18}\ \frac{W}{m^2}$ that almost equal to 5 kJ output.
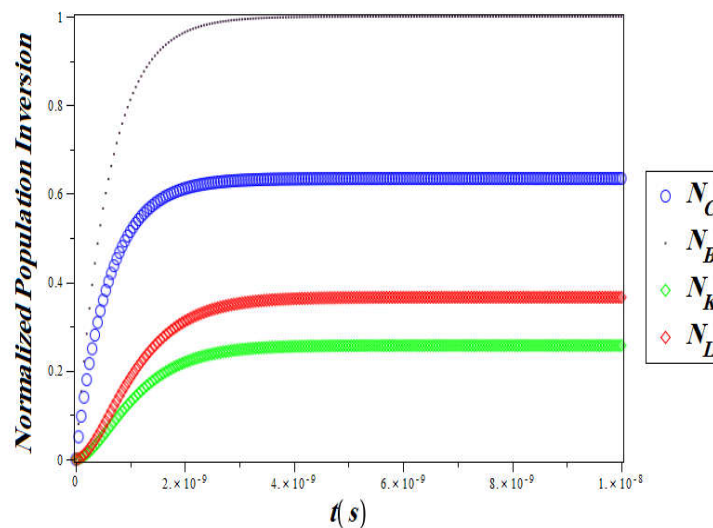

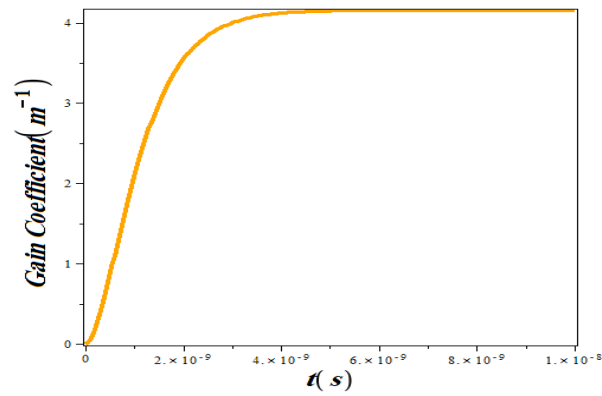Figure 2: Population inversion of levels B, C and the levels of vibration

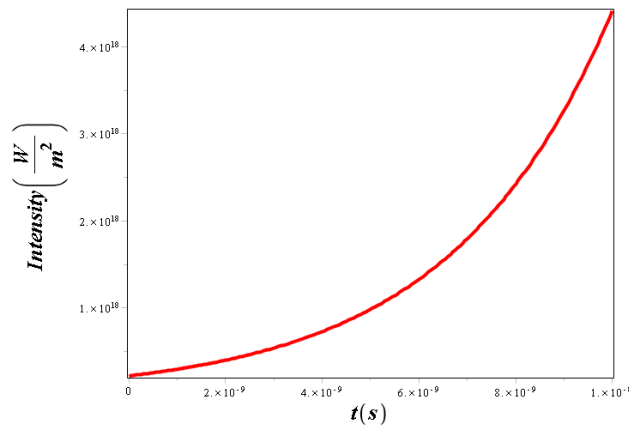Figure 3: Gain recovery curve for KrF amplifier.

Figure 4: Output intensity KrF laser pulse

4-Relativistic piston laser model analysis

In ICF the ponderomotive force of intense electromagnetic pulses is considered for many years as a promising way to accelerate matter up to relativistic velocities. The ponderomotive force of intense electromagnetic pulses is considered for many years as a promising way to accelerate matter up to relativistic velocities. The ponderomotive force acceleration can be also efficient in bulk targets, where the electrons are pushed steadily by the radiation pressure and the ions following behind them build up the double layer structure supported by the ponderomotive force. Protons or heavy ions accelerated in the ponderomotive regime may serve as drivers for efficient plasma heating of high-energy density states, or for the preparation of warm dense matter conditions on a sub-picosecond time scale. As a further possible application of this regime we considered the fast ignition of thermonuclear fusion targets by using a two short and intense laser pulses. There are two qualitatively different regimes of the relativistic laser pulse propagation through a dense plasma. The regime of induced transparency is commonly related to plasma densities below or slightly above the critical density. For higher densities, such a strong laser pulse experiences the stimulated Raman scattering, self-focusing and self-modulation. The laser pulse propagation becomes unstable and is accompanied by high energy losses. Another regime is realized in a strongly over-dense plasma. Here, the laser pulse ponderomotive force pushes electrons ahead producing a cavitation zone. The electron density peak reflects the laser pulse and the charge separation field pulls the ions forward. As a result, the interaction of an ultra-intense laser pulse with a high-density plasma forms a double layer structure (often called a laser piston) that separates the propagation path of the laser pulse,

where there is no plasma, from a shocked plasma with no laser pulse. Figure5 displays the structure of the piston obtained from the analytical model.
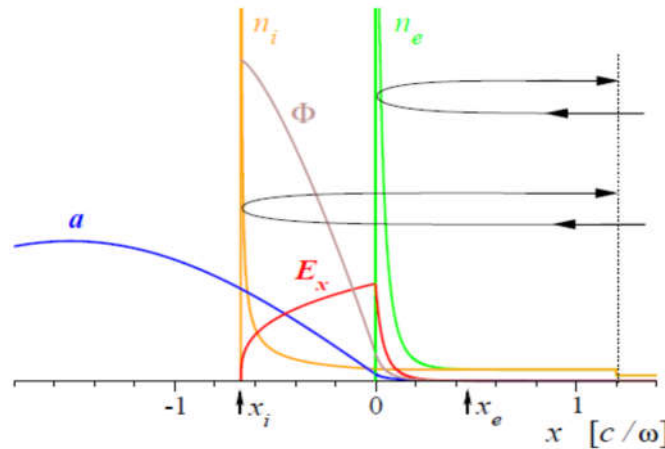

Figure 5: Double layer structure of the laser piston maintained by the radiation pressure: laser field amplitude – dot-dashed line (blue), laser intensity – thin solid (brown), electron density – dashed (green), electrostatic field – thick solid (red), ion density –solid (black).

In the reference frame of the double layer, the dimensionless vector potential for a circularly polarized laser pulse represents a standing wave with the amplitude $2a_0$ in the downstream region. The unperturbed ion density n_{0i} is upstream, $x' > x'_s >$. At position $x' = x'_s$, the ion density undergoes a jump from n_{0i} to $2n_{0i}$. In the interval between, $0 < x' < x'_s$, there is an overlap of the particles moving towards the piston and reflected from it. The ions are decelerated passing from $x' = 0$ to $x' = x'_i$. Then they reverse their motion and are accelerated from the piston. These two steps correspond in the laboratory frame to acceleration from a zero velocity to the velocity v_f and then to v_i. Let us first recall the expression for the piston velocity, which follows from the conservation relations. We assume that neither electrons nor ions are heated in the interaction zone. In the reference frame of the piston moving with the velocity $v_j = \beta_j c$, the laser light is Doppler downshifted. The frequency in the moving frame ω'_0 is related to the frequency in the laboratory frame ω_0 by the Lorentz transformation, $\omega'_0 = \omega_0 \gamma_f (1 - \beta_f)$, where $\gamma_f = (1 - \beta^2_f)^{-1/2}$. The laser light is completely reflected from the plasma and the momentum flux deposited by the photons in the moving frame is $\frac{2I'}{c}$. Here, I' is the light intensity in the piston frame related to the incident laser intensity I in the laboratory frame by the Lorentz transformation, $I' = I(1 - \beta_f)/(1 + \beta_f)$. This photon momentum flux has to be balanced by the pressure of particles coming from the right side with the piston velocity (they are at rest in the laboratory system) and reflected back elastically. The particle momentum flux in the piston reference frame reads $2n'_i v_f m_a \gamma_f v_f = 2\rho c^2 \gamma^2_f \beta^2_f$, where $m_a = m_i + Z m_e$ the atomic mass is, n_{0i} is the upstream ion density in the laboratory frame, Ze is the ion charge, and $\rho = m_a n_{0i}$ is the mass density. Then, by equating the momentum fluxes of photons and those of ions and electrons, one finds the relation for the front velocity:

$$\frac{I}{\rho c^3} \frac{1 - \beta_f}{1 + \beta_f} = \gamma^2_f \beta^2_f \qquad (6)$$

Solving Eq. (6) for the piston velocity, we have:

$$\beta_f = \frac{B}{1+B} \qquad (7)$$

where $B = (I / \rho c^3)^{1/2}$. It is convenient to relate the laser intensity to the dimensionless field amplitude a_0, $I = \alpha a_0^2 n_c m_e c^3$. Here, α=1 in the case of circular polarization and α =1/2 in the case of linear polarization. The three-dimensional diagram of Fig. 6 shows that increasing the range of the laser and decreasing the density of the plasma ion, increase the piston speed.
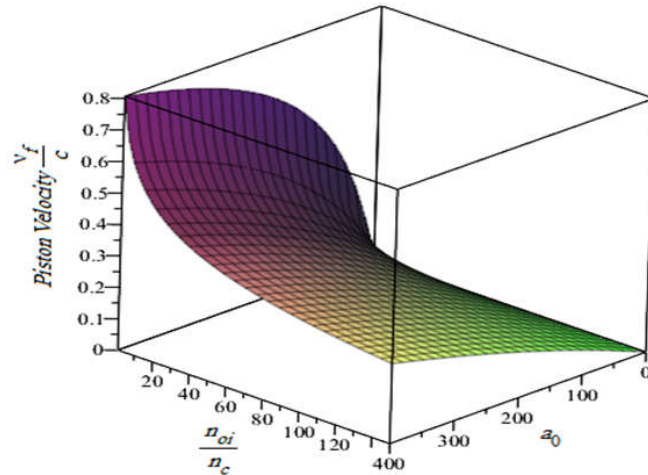

Figure.6. 3D piston speed variation in terms of ion density and vector potential for laser pulses with circular polarization in plasma D-^{3}He

Then we have $B = a_0 \sqrt{\alpha n_c m_e / n_{0i} m_a}$. In particular, for $B \ll 1$ the piston is nonrelativistic and one finds the known formula: $\beta_f \cong B$, while in the ultrarelativistic case, $B \gg 1$, the piston gamma factor increases as the square root of the laser amplitude: $\gamma_f \cong \left(B/2\right)^{\frac{1}{2}}$. After applying the Lorentz transformation to the velocity of ions reflected from the piston, we get the expression $v_i = 2\beta_f c / \left(1 + \beta_f^2\right)$ in the laboratory frame. The corresponding ion kinetic energy reads:

$$\varepsilon_i = m_i c^2(\gamma_i - 1) = 2m_i c^2 \gamma_f^2 \beta_f^2 = 2m_i c^2 \frac{B^2}{1+2B} \qquad (8)$$

The three-dimensional of Fig. 7 shows that increasing the range of the laser and decreasing the density of the plasma ion increase the kinetic energy of the ion. Assuming that no energy is deposited in electrons.
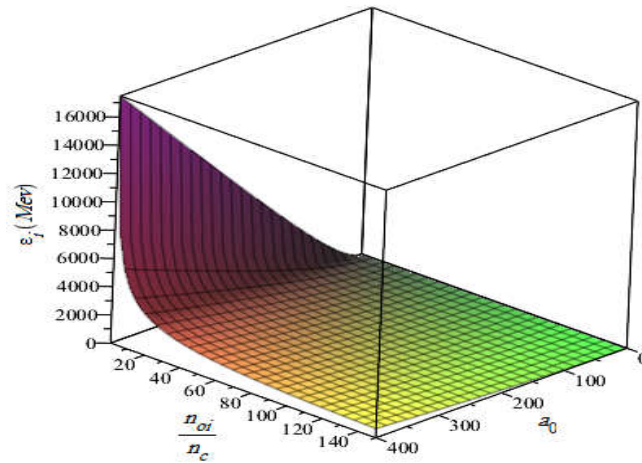
Figure.7.3D variations of kinetic energy of ion in terms of ion density and amplitude of the vector potential of laser pulses with polarization in plasma D-^{3}He

In the case $B \ll 1$, the ion gains the energy $\varepsilon_i \cong 2m_i c^2 B^2$, while in the ultra-relativistic case, $B \gg 1$, $\varepsilon_i \cong m_i c^2 B$. Knowing the piston velocity, we can also determine the reflection coefficient of the laser light in the laboratory frame:

$$R = \frac{(1 - \beta_f)}{(1 + \beta_f)} \qquad (9)$$

And the energetic efficiency of the laser driven ion acceleration:

$$1 - R = \frac{2B_f}{1 + B_f} = \frac{2B}{1 + 2B} \qquad (10)$$

The three-dimensional of Fig. 8 shows that the magnitude of the refractive index increases with decreasing the laser range and increasing the density of the plasma.
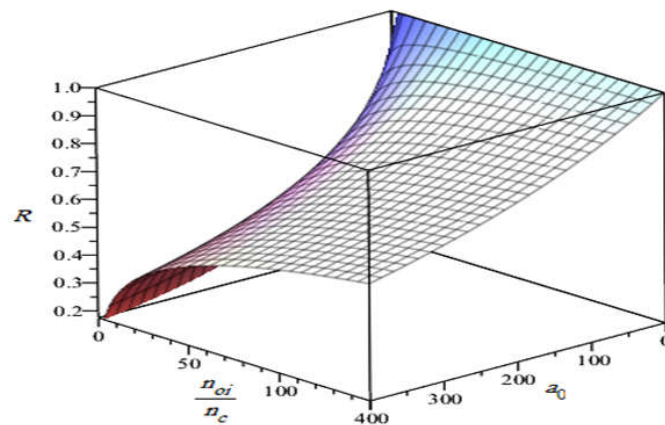

Fig.8: 3D variations of the reflectance coefficient in terms of the ion density and amplitude of the vector potential of laser pulses with circular polarization in the plasma D-^{3}He

Let us consider plasmas with an arbitrary density profile. The equation for the piston coordinate reads $\frac{dx_p}{dt} = v_f$. By integrating this equation over the plasma length, one finds the time $T_b = \int \frac{dx}{v_f}$ needed for the laser pulse propagation through the plasma. For a monotonic plasma

density profile, increasing from ρ_{min} min to ρ_{max}, one can write: $dx/L = d\rho/\rho$, where $L = \rho/\left(d\rho/dx\right)$ is the density scale length. Then:

$$T_b = \int \frac{L d\rho}{v_f \rho} \qquad (11)$$

In case of an arbitrary density profile, this formula can be integrated numerically. For an exponential dependence $\rho(x)$, where L is a constant, one finds the expression:

$$T_b = \frac{2L}{c}\left[\left(\frac{1-\beta_{f\,max}}{\beta_{f\,max}} - \frac{1-\beta_{f\,min}}{\beta_{f\,min}}\right) + \ln\left(\frac{\beta_{f\,min}}{\beta_{f\,max}}\frac{1-\beta_{f\,max}}{1-\beta_{f\,min}}\right)\right] \qquad (12)$$

Where $\beta_{f\,max}$ and $\beta_{f\,min}$ are the front velocities at the maximum and minimum densities. In terms of laser intensity and plasma density, we can rewrite this result as:

$$T_b = 2L\sqrt{\frac{c}{I}}\left(\sqrt{\rho_{max}} - \sqrt{\rho_{min}}\right) + \frac{L}{c}\ln\frac{\rho_{max}}{\rho_{min}} \qquad (13)$$

From Eq. (13) it becomes visible that the second term in Eqs. (12) and (13) represents the time T_v needed for light to traverse the distance L_p, $T_v = \int dx/c = \int L d\rho/\rho c = L_p/c$, where L_p is the plasma layer thickness. Supposing a nonrelativistic piston motion, we obtain the simpler relation:

$$T_b \cong (2L/c)\left(1/\beta_{f\,max} - 1/\beta_{f\,min}\right) + L_p/c \qquad (14)$$

Since for the cases of interest $\beta_{f\,max} \ll \beta_{f\,min}$, the burn through time, according to Eq. (14), is roughly proportional to the density scale length, the square root of maximum density and it is inversely proportional to the laser amplitude (see also Eq. (13)). In addition, one can find the laser pulse duration T_p needed to penetrate into the plasma up to a given density. The corresponding formula reads:

$$T_p = T_b - T_v = \frac{1}{c}\int\frac{L d\rho}{B_\rho} = \sqrt{\frac{c}{I}}\int\frac{L d\rho}{\sqrt{\rho}} \qquad (15)$$

In particular, for the exponential density profile we get: $T_p \cong 2L\left(\rho_{max}\,c/I\right)^{1/2}$, $T_p = 2L\left(c/I\right)^{\frac{1}{2}}\left(\sqrt{\rho_{max}} - \sqrt{\rho_{min}}\right)$. Laser pulse durations T_p calculated with help of this relation for a set of laser amplitudes a_0 and plasma scale lengths L, normalized to the laser wavelength $\lambda_0 = 2\pi c/\omega_0$, in dependence on the plasma density, n_{0i}/n_c. The three-dimensional of Figure 9 shows that the laser pulse time increases with decreasing the laser range and increasing the density of the plasma.
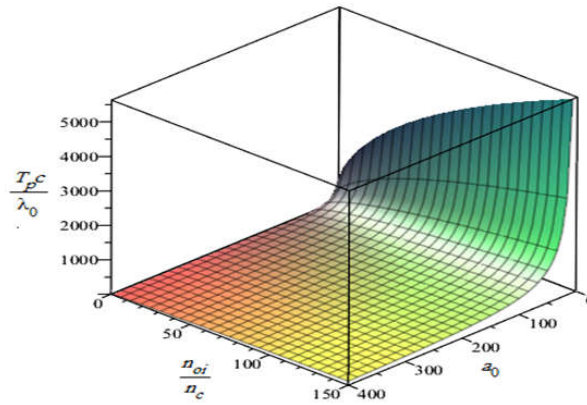
Figure 9:3D variations of laser pulse time in terms of ion density and the potential for vector pulses for circular polarization pulses and L=20λ_0 in D-^{3}He plasma

In the case of a homogeneous plasma layer, the laser pulse duration needed for hole boring is linearly proportional to the plasma length, $T_p = {L_p}/{\beta_f c} - {L_p}/{c} = {L_p}/{Bc}$. The product of pulse duration T_p and laser intensity I gives the laser fluence, $F_{las} = IT_p$, used to push plasma over the length L_p. As there is no plasma left behind the piston, this process can be considered as a laser-assisted hole boring in an overdense plasma.

The piston model also allows to find an expression for the energy distribution of accelerated ions. During the time interval dt the piston crosses the distance $v_f dt$ and accelerates $dN_i = n_{0i} v_f dt$ ions. These ions are distributed in the energy interval $d\varepsilon_i = \left(\frac{d\varepsilon_i}{dx}\right) v_f dt$. Taking into account that the ion energy depends on β_f and therefore on the plasma density, one finds the following formula for the ion energy spectrum in the case of the exponential density profile:

$$\frac{dN_i}{d\varepsilon_i} = \frac{L}{m_a}\left|\frac{d\varepsilon_i}{d\rho}\right|^{-1} = \frac{IL}{2m_a m_i c^5 \beta_f^4 \gamma_f^6 (1+\beta_f)} \qquad (16)$$

Where $\beta_f^2 = {\varepsilon_i}/{(2m_i c^2 + \varepsilon_i)}$ is related to the ion energy according to Eq. (8). Figure 10 shows that with the reduction of kinetic energy of the ion and the increase of the laser range, the amount of energy distribution of the ions accelerates.
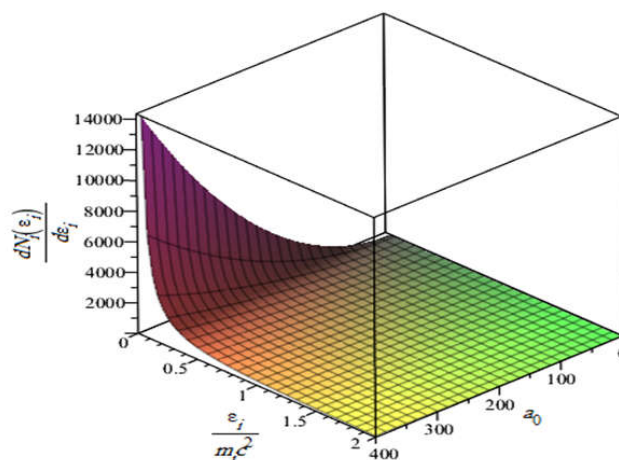
Figure 10:3D variations of energy distribution of ions in terms of kinetic energy of ions and different amplitudes of circular polarization of laser in D-^{3}He exponential plasma layer with L=$20\lambda_0$

Fig. 11, shows that the two-dimensional variations of the mean, maximum and minimum ion kinetic energy in terms of the laser range with circular polarization in the DT plasma with $\rho_{max} = 100\rho_c$ and $\rho_{min} = 5\rho_c$. From this figure we see that ,with increasing range of lasers, all three quantities, the average, the maximum and the half of the kinetic energy of the ion increases. The average of the kinetic energy of the ions is almost twice as high as half the energy.
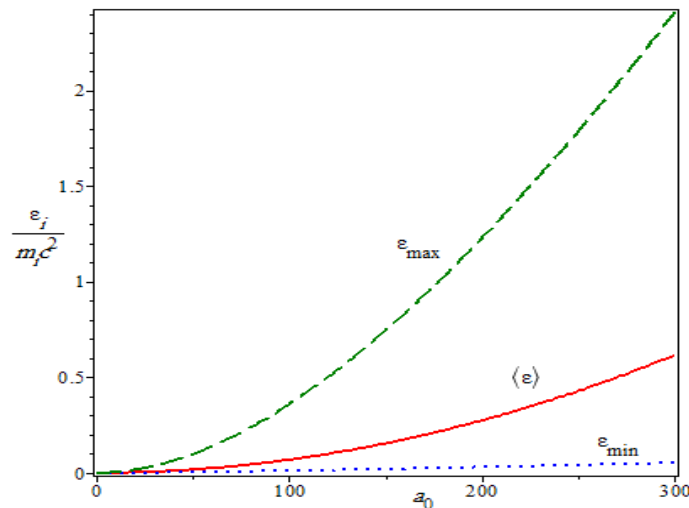

Fig. 11: Variations of the mean, maximum and minimum ion kinetic energy in terms of the laser range with circular polarization in the plasma D-^{3}He with $\rho_{max} = 100\rho_c$ and $\rho_{min} = 5\rho_c$

The conservation of the ion particle flux provides a relation between the ion density and ion velocity for incoming and reflected ions. The ion energy conservation, $\varepsilon_i' + Ze\varphi' = m_i c^2(\gamma_f - 1)$, provides the value of the potential jump in this layer, $Ze\varphi'(x_i') = m_i c^2(\gamma_f - 1)$, needed to stop and reflect the ions. The distribution of the electrostatic potential follows from the Poisson equation rewritten as an equation for the ion relativistic factor in the piston reference frame:

$$\frac{d^2\gamma_i'}{dx'^2} = \frac{2\omega_{pi}^2 \gamma_f}{c^2} \frac{\beta_f}{\beta_i'} \quad (17)$$

Where $\beta_i' = \left(1 - \gamma_i'^{-2}\right)^{1/2}$ and $\omega_{pi} = \left(Z^2 e^2 n_{0i}/m_i \epsilon_0\right)^{1/2}$ is the upstream ion plasma frequency. Then the first integral of Eq. (17) provides a relation between the electric field and the ion energy in the charge separation layer. In particular, at the position of the electron peak the electrostatic field reads:

$$E_x(0) \cong \frac{2}{Ze} m_i c \omega_{pi} \gamma_f \beta_f = 2\sqrt{\alpha} E_0 \sqrt{\frac{1-\beta_f}{1+\beta_f}} \quad (18)$$

The expression (18) shows that the maximum electrostatic field in the piston is approximately equal to twice the electric field of the incident laser pulse at small piston velocities. By integrating Eq. (17) once more, we define the position of the ion turning point and the thickness

of the ion sheath layer, $\Delta_i' = -x_i'$. In the non-relativistic piston regime, $\beta_f \ll 1$, the width of the ion separation layer is $\Delta_i = \gamma_f \Delta_i' \approx {v_f}/{3\omega_{pi}}$. The dependence of the thickness of the ionic layer on the parameter γ_f is depicted in Fig. 12.
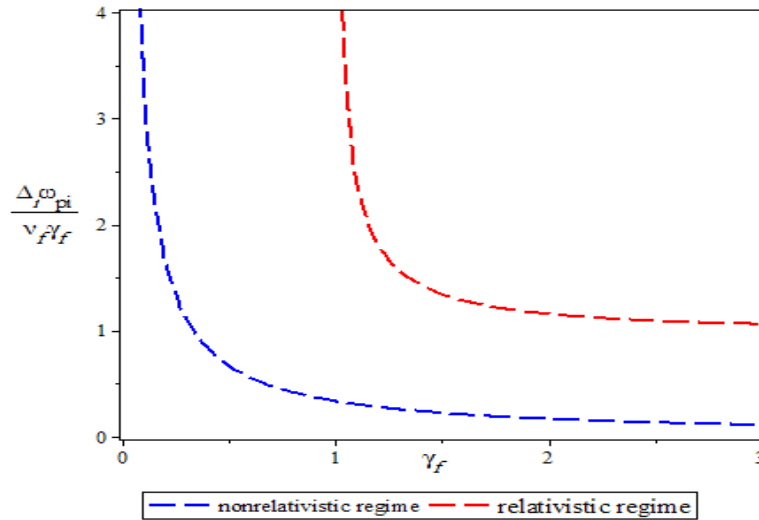

Fig.12: Two-dimensional variations of the thickness of the ion charge separation layer (normalized with $({v_f \gamma_f}/{\omega_{pi}})$) in terms of the piston relativistic factor γ_f

One can also find the ion circulation time in the charge separation layer:

$$t_i = \gamma_f t_i' = \frac{1}{\omega_{pi}} \sqrt{\frac{\gamma_f}{\beta_f}} \int_1^{\gamma_i'(0)} \frac{d\gamma_i' \gamma_i'}{(\gamma_i'^2-1)^{3/4}} \cong \frac{2\gamma_f}{\omega_{pi}} \quad , \text{because } \gamma_f \approx \gamma_i'(0).$$

Figure 13 shows that the ion rotation time in a separate layer of load increases with increasing ion density and decreasing the amplitude.
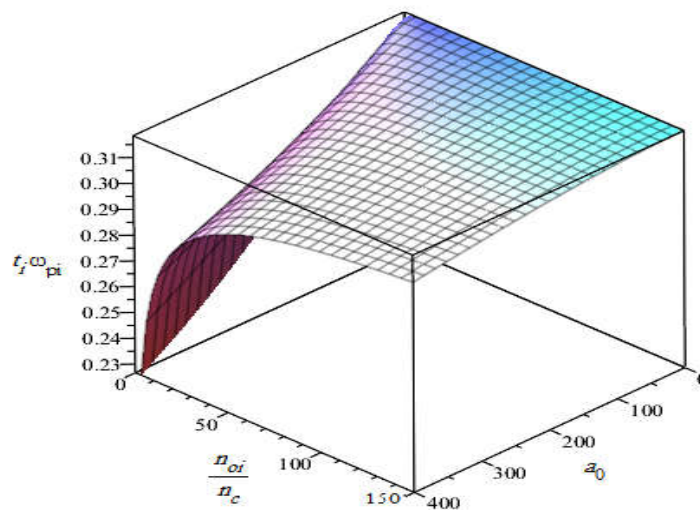

Fig.13: 3D variations of the ion rotational time in terms of density in a separate load layer and the amplitude of the laser with circular polarization in plasma D-^{3}He

In the non-relativistic piston regime, $\beta_f \ll 1$, it depends only on the ion plasma frequency. Next we investigate the structure of the electron sheath layer $[0, x'_e)$ ٫ and the laser intensity profile near the turning point of electrons, $x' = 0$, coming from the upstream region. In analogy to ions, the electron density distribution follows from the continuity equation. For the incoming electrons we have $n'_e - v'_{x-,e} = -Z n_{0i} \gamma_f v_f$, and for the reflected electrons, $n'_{e+} v'_{x+,e} = Z n_{0i} \gamma_f v_f$. correspondingly, there are two electron streams with the opposite velocities within the electron sheath layer, and for the entire electron density we get:

$$n'_e = 2 Z n_{0i} \gamma_f \frac{\beta_f}{\beta'_{x,e}} \qquad (19)$$

Although the potential drop in the electron sheath layer is relatively small compared to that we found above in the ion charge layer, one has to account for the influence of the electrostatic field on the ion motion inside the electron sheath. Then the ion density becomes $n'_i(x') = 2 \left. \frac{n_{0i} \gamma_f \beta_f}{\beta'_i(x')} \right.$. As the electrons and ions are moving in the same electrostatic potential, one finds the relation between their γ-factors:

$$\gamma'_i(x') = \gamma_f - \frac{Z m_e}{m_i}[\gamma'_e(x') - \gamma_f] \qquad (20)$$

The electron gamma factor $\gamma'_e(x') = \left[1 + \left(\frac{p'_{x,e}}{m_e c^2}\right)^2 + \left(\frac{p'_{\perp,e}}{m_e c^2}\right)^2\right]^{1/2}$ obeys the energy conservation:

$$\varepsilon'_e = m_e c^2(\gamma'_e - 1) = e\phi' + m_e c^2(\gamma_f - 1) \quad (21)$$

Which assumes that the laser field is zero to the right from the electron sheath layer at $x' \geq x'_e$. Since the perpendicular component of the electron momentum is defined by the laser field, $p_{\perp,e} = a m_e c$, the expression for the electron longitudinal velocity reads:

$$v'_{x\pm,e} = \pm c\sqrt{1 - (1 + a^2)/\gamma'^2_e} \qquad (22)$$

The electron density is described by the Poisson equation in the form:

$$\epsilon_0 \frac{d^2\varphi'}{dx'^2} = 2 Z e n_{0i} \gamma_f \left(\frac{\beta_f}{\beta'_{x,e}} - \frac{\beta_f}{\beta'_i}\right) \qquad (23)$$

Where the electron and ion densities have been substituted by their expressions specified above. Applying the equation of electron motion in stationary approximation, we derive an equation for the electron relativistic factor:

$$\frac{d^2\gamma'_e}{dx'^2} = 2\frac{\omega^2_{pe}}{c^2}\gamma_f \beta_f \left(\frac{\gamma'_e}{\sqrt{\gamma'^2_e - 1 - a^2}} - \frac{\gamma'_i}{\sqrt{\gamma'^2_i - 1}}\right) \qquad (24)$$

The boundary conditions to be fulfilled are $\gamma'_e(0) = [1 + a^2(0)]^{1/2}$, containing the transverse momentum of the electrons at the electron turning point, $\beta'_{x,e}(0) = 0$, with the laser field amplitude (0) and $\gamma'_e(x'_e) = \gamma_f$ on the right of the electron sheath. Furthermore, we know the values of the electrostatic field in the unperturbed plasma, $0 = E_x(x' \to \infty)$, and at $x' = 0$:

$$eE_x(0) = 2m_e \omega_0 c \sqrt{\frac{m_i n_{0i}}{m_e n_c}}\sqrt{\gamma_f \beta_f}[\gamma'^2_i(0) - 1]^{1/4} \qquad (25)$$

Since the electric field must change continuously from the charge separation layer to the electron sheath, the latter expression was deduced from the maximum field in the ion layer. Equation (25) is now corrected in comparison with Eq. (18) for the ion energy change in the electron sheath.
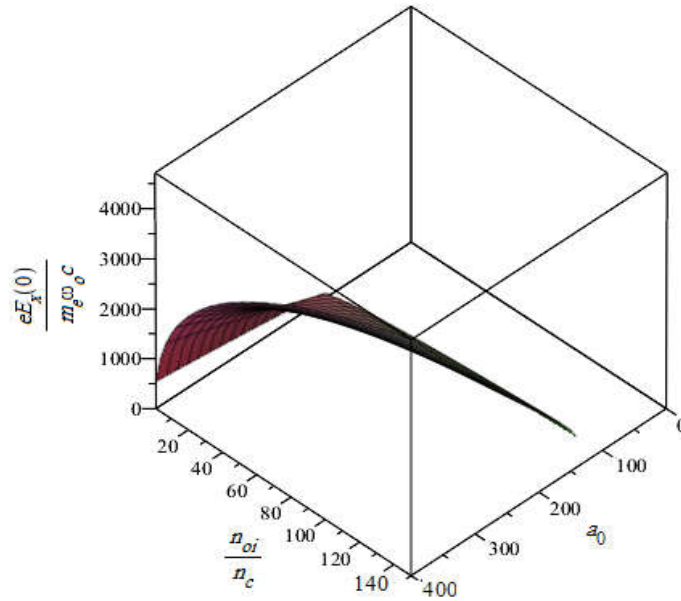
Fig.14:3D variations of electrostatic field in terms of the density and amplitude of the laser with circular polarization in non-turbulent plasma D-^{3}He

Using the relation: $eE_x = -m_e c^2 \, d\gamma'_e/dx'$, which follows directly from the electron energy conservation law, one finds also a condition for the electron gamma factor on the left boundary of the electron sheath:

$$\frac{d\gamma'_e}{dx'}\big|_{x'=0} = -2\sqrt{\frac{m_i}{Zm_e}}\frac{\omega_{pe}}{c}\sqrt{\gamma_f \beta_f}[\gamma_i'^2(0)-1]^{1/4} \qquad (26)$$

Equation (24) for the electron energy has to be complemented with the field equation for the laser wave. On the left from the electron sheath layer, $x' < 0$, the laser does not interact with particles so the amplitude a verifies the equation for the standing electromagnetic wave in vacuum written in the piston frame:

$$\frac{d^2 a}{dx'^2} = -\frac{\omega_0^2}{c^2}\frac{1-\beta_f}{1+\beta_f}a \qquad (27)$$

This equation can be easily integrated and the integration constant is defined by the condition of total reflection in the piston reference frame. We obtain the result:

$$\left(\frac{da}{dx'}\right)^2\big|_{x'=0} + \frac{\omega_0^2}{c^2}\frac{1-\beta_f}{1+\beta_f}a^2(0) = 4\frac{\omega_0^2}{c^2}\frac{1-\beta_f}{1+\beta_f}a_0^2 \qquad (28)$$

Where a_0 is the dimensionless amplitude of the vector potential of the incident wave in the laboratory frame.

To the right from the electron turning point one has to account for the electron screening effect, and the equation for the evanescent laser field reads:

$$\frac{d^2 a}{dx'^2} = \left(\frac{e^2 n'_e}{\epsilon_0 m_e \gamma'_e c^2} - \frac{\omega_0^2}{c^2}\frac{1-\beta_f}{1+\beta_f}\right)a \qquad (29)$$

With help of Eqs. (19) and (22), this wave equation takes the final form:

$$\frac{d^2 a}{dx'^2} = 2\frac{\omega_{pe}^2}{c^2}\frac{\beta_f a}{\sqrt{\gamma_e'^2-1-a^2}} - \frac{\omega_0^2}{c^2}\frac{1-\beta_f}{1+\beta_f}a \qquad (30)$$

The system of coupled Eqs. (24) and (31) has one first integral that can be found as follows. One multiplies Eq. (24) by $d\gamma'_e/dx'$ and integrates it over the interval $x' \epsilon [0, \infty)$. Then one

multiplies Eq. (30) by: $\frac{da}{dx'}$, integrates over the same interval, and subtracts both resulting equations from each other. Applying the boundary conditions (26) and (28), one finds a relation between a_0 and γ_f. One may also apply the boundary conditions (18) and (28) and the momentum flux conservation (6) in an attempt to estimate the value of the vector potential $a_0 \cong \gamma_f \beta_f$. However, such a relation would be incorrect as one has to account for the interaction of upstream ions with the electrostatic field in the electron sheath. The correct relation (25) for the maximum electrostatic field provides a more appropriate estimate for the vector potential and the electron energy at the electron turning point:

$$a(0) \cong \gamma_e'(0) \cong \gamma_f\left(1 + \beta_f^2\sqrt{2m_i/Zm_e}\right) \qquad (31)$$

To integrate the system of coupled Eqs. (24) and (30) numerically, we determine first the asymptotic solution to the right from the electron sheath at $x' \gg {}^c/_{\omega_{pc}}$, supposing $\gamma_e' = \gamma_f + \delta\gamma$ and $_\jmath \, \delta\gamma, a(x') \ll 1$. The linearized system reads:

$$\gamma_f\beta_f^2 \frac{d^2\delta\gamma}{dx'^2} = \frac{\omega_{pe}^2}{c^2}\left(-2\frac{\delta\gamma}{\gamma_f} + a^2\right) \qquad (32)$$

$$\frac{d^2a}{dx'^2} = 2\frac{\omega_{pe}^2}{c^2}a - \frac{\omega_0^2}{c^2}\frac{1-\beta_f}{1+\beta_f}a \qquad (33)$$

Equation (32) contains a^2 as a source term. Therefore, this equation does not contain any free constants, $\delta\gamma$ is of the same order of magnitude as a^2 and it follows from a particular solution to Eq. (32). Consequently, the asymptotic solution is defined by only one constant that follows from the evanescent solution to Eq. (33):

$$a(x') = a_\infty exp\left(-\sqrt{2q}\frac{x'\omega_{pe}}{c}\right) \qquad (34)$$

Where $q = 1 - \dfrac{\left(\omega_0^2/2\omega_{pe}^2\right)(1-\beta_f)}{(1+\beta_f)} \cong 1$. Using the asymptotic solution, one can solve now the full nonlinear systems (24) and (30) numerically by starting the integration procedure from the aperiodic part of the asymptotic solution as a boundary condition at large values x_∞'. For a given small value of the evanescent amplitude a_∞, we vary the corresponding coordinate x_∞' as long as the boundary conditions in the final point $x' = 0$ are not satisfied with sufficiently high accuracy. Figure 15 shows that electrostatic potential energy increases at the location of the electron peak by decreasing the ion density and increasing the amplitude.
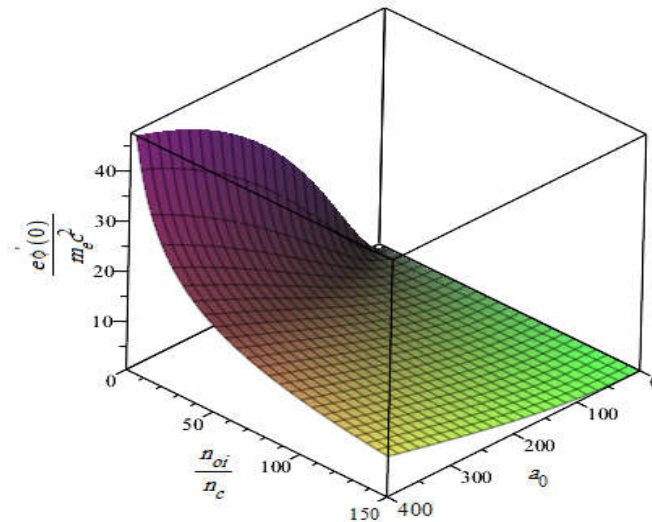
Figure 15:3D variations of electrostatic potential energy in the location of electron peak in terms of plasma density and pulsed amplitude of the incident laser with circular polarization in D-^{3}He plasma

However, the electrostatic potential at the position of the electron peak is different from zero:

$$e\phi'(0) = m_e c^2 \left[\sqrt{1 + a^2(0)} - \gamma_f\right] \qquad (35)$$

The same expression could be obtained from the energy conservation law for the ions in the charge separation zone if one would account for the deceleration of ions in the electron sheath. However, $e\varphi'(0)$ is much smaller than the maximum value of the electrostatic potential at the ion turning point, $e\varphi'_{max} = {m_i c^2 (\gamma_f - 1)}/{Z}$, and this approximation has a little effect on the ion charge layer characteristics. The correct relation (36) provides the monotonic decrease of the potential with increasing x' from a maximum value at x'_i on the left boundary of the ion charge separation layer to zero on the right boundary of the electron sheath. Therefore, the stationary electrostatic field E_x is always positive. Figure 16 shows the maximum electrostatic potential energy at the location of the electron peak, which increases with decreasing ion density and increasing the amplitude.
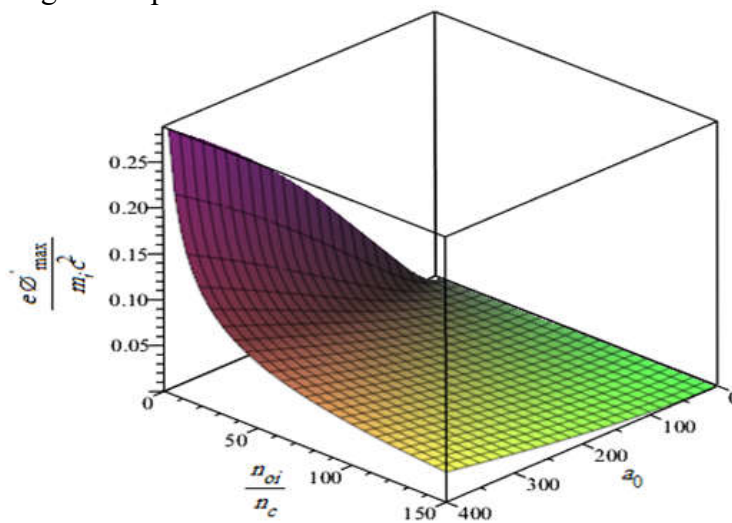

Figure 16:3D variations of maximum electrostatic potential at the turning point (ion rotation) based on the plasma density and the pulsed amplitude of the incident laser with circular polarization in the plasma D-^{3}He

5. Conclusion

In the first step of this work we solve the dynamics equations of Krypton-Fluoride (KrF) laser with an operating wavelength of 248 nm has the deepest ultraviolet (UV) wavelength of all current candidates for laser drivers. These qualities provide fundamental advantages to obtaining robust high gain implosions by means of direct drive. Then in the second step, using the obtained expression for the piston velocity, we determine the energy of the accelerated ions, their energy distribution, and the laser penetration depth in case of an inhomogeneous plasma slab. By this method we can estimate the laser parameters necessary for propagating the light wave up to a certain density. Moreover, we present solutions for the governing equations describing the detailed structures of the ion charge separation layer and the electron sheath of the piston. Results of our work were presented for circular polarization and various intensities of the incident laser light, which exposes homogeneous plasma slabs of different densities. Although the calculations confirm the basic features of the analytical model, they show two overlaying nonstationary effects: nonlinear oscillations of the piston parameters around the stationary values and strong radiative energy losses of accelerated electrons in ultra-intense laser fields at low plasma density. These nonstationary features modify the stationary piston regime and set the limits on its validity.

References

[1] BODNER, S.E., et al., "Overview of new high gain target design for a laser fusion power plant", Fusion Eng. Des. 60 1 (2002) 93.

[2] BETTI, R., et al., "Shock ignition of thermonuclear fuel with high areal density", Phys. Rev. Lett. 98 15 (2007) 155001.

[3] PERKINS, L. J., et al., "Shock ignition: a new approach to high gain inertial confinement fusion on the National Ignition Facility", Phys. Rev. Lett. 103 4 (2009) 045004. [4] SCHMITT, A. J., et al., "Direct drive fusion energy shock ignition designs for sub-MJ lasers", Fusion Sci. Tech. 56 1 (2009) 377.

[5] OBENSCHAIN, S. P., et al., "The Nike KrF laser facility: performance and initial target results", Phys. Plasmas 3 5 (1996) 2098.

[6] LEHMBERG, R. H., OBENSCHAIN, S. P., "Use of induced spatial incoherence for uniform illumination of laser fusion targets", Optics Commun. 46 1 (1983) 27.

[7] LEHMBERG, R. H., GOLDHAR, J., "Use of incoherence produce smooth and controllable irradiation profiles with KrF fusion lasers", Fusion Tech. 11 3 (1987) 532.

[8] SETHIAN, J. D., et al., "Electron beam pumped KrF lasers for fusion energy", Phys. Plasmas 10 5 (2003) 2142.

[9] Wurzel, S. E. and Hsu, S. C. (2022). Progress toward fusion energy breakeven and gain as measured against the Lawson criterion. *Physics of Plasmas*, 29(6):062103.

[10]Hora, H., Eliezer, S., and Nissim, N. (2021). Elimination of secondary neutrons from laser proton-boron fusion. *Laser and Particle Beams*, 2021:1–3.

[11]Putvinski, S., Ryutov, D., and Yushmanov, P. (2019). Fusion reactivity of the pB-11 plasma revisited. *Nuclear Fusion*,59(7):076018.

[12] Roohalah Mirzaeian, Seyedeh Nasrin Hosseinimotlagh∗, Mahboobeh Shaghaghian," Investigation of key phenomena in increasing the fusion energy gain of neutron-free fuel", Radiation Physics and Engineering 2023; 4(3):53–64

[13]Dodder, D. and Gammel, J. (1952). Elastic scattering of protons and neutrons by helium. *Physical Review*, 88(3):520

[14] Eliezer, S., Hora, H., Korn, G., et al. (2016). Avalanche proton-boron fusion based on elastic nuclear collisions.*Physics of Plasmas*, 23(5):050704.

[15] Hay, M. J. and Fisch, N. J. (2015). Ignition threshold for non-Maxwellian plasmas. *Physics of Plasmas*, 22(11):112116.

[16] Sikora, M. and Weller, H. (2016b). A new evaluation of the $B^{11}(p, \alpha)\alpha\ \alpha$ reaction rates. *Journal of Fusion Energy*,35(3):538–543.

[17] Sikora, M. and Weller, H. (2016a). A new evaluation of the $^{11}B(p,\alpha)\alpha\ \alpha$ reaction rates. *Journal of Fusion Energy*,35(3):538–543.